mater.scichina.com link.springer.com

Published online 12 March 2021 | https://doi.org/10.1007/s40843-020-1599-2
Sci China Mater 2021, 64(8): 1952–1963

Portable wastewater treatment system based on synergistic photocatalytic and persulphate degradation under visible light

Meng Zu[1], Shengsen Zhang[2*], Changyu Liu[3], Porun Liu[1], Dong-Sheng Li[4], Chao Xing[1,5] and Shanqing Zhang[1*]

ABSTRACT **Highly efficient, low-cost, and portable wastewater treatment and purification solutions are urgently needed for aqueous pollution removal, especially at remote sites. Synergistic photocatalytic (PC) and persulphate (PS) degradation under visible light offers an exceptional alternative for this purpose. In this work, we coupled a TiO_2-based PC system with a PS oxidation system into a portable advanced oxidation device for rapid and deep degradation of organic contaminants in wastewater. Using hydrogenation, we fabricated hydrogenated anatase branched-rutile TiO_2 nanorod (H-AB@RTNR) photocatalysts which enable the PC degradation to occur under visible light and improve the utilization of solar energy. We also discovered that the addition of PS resulted in the synergistic degradation of tenacious and persistent organics, dramatically improving the extent and kinetics of the degradation. A degradation rate of 100% and a reaction rate constant of 0.0221 min^{-1} for degrading 1 L rhodamine B (20 mg L^{-1}) were achieved in 120 min in a specially designed thin-layer cell under visible light irradiation. The superior performance of the synergistic PC and PS degradation system was also demonstrated in the degradation of real industrial wastewater. Both remarkable performances can be attributed to the heterophase junction and oxygen vacancies in the photocatalyst that facilitate the catalytic conversion of PS anions into highly active radicals ($\cdot SO_4^-$ and ·OH). This work suggests that the as-proposed synergistic degradation design is a promising solution for building a portable wastewater treatment system.**

Keywords: synergistic effect, hydrogenated TiO_2, oxygen vacancies, persulphate, thin-layer cell, real wastewater

INTRODUCTION

Toxic chemical dyes are frequently used in the textile industry and have severe implications for environmental and human health [1,2]. For some remote textile plants, highly efficient, scalable, portable, and low-cost devices for wastewater treatment and purification are urgently needed [3]. Among numerous wastewater treatment and purification methods, synergistic photocatalytic (PC) and persulphate (PS) degradation technologies (PC-PS) have aroused enormous attention due to their potent degradation ability of tenacious dye contaminants [4,5]. The synergistic effects between PC and PS anions can be explained by two mechanisms. Firstly, the photogenerated electrons (e^-) from the PC process can effectively convert PS anions ($S_2O_8^{2-}$, E^0 = 2.01 V *vs.* normal hydrogen electrode (NHE)) to sulphate radicals ($\cdot SO_4^-$, E^0 = 2.60 V *vs.* NHE), which enhances the degradation performance. Secondly, the consumption of e^- by the activation process of $S_2O_8^{2-}$ can facilitate the separation of photogenerated electron-hole pairs, which in turn enhances the PC performance [6]. Accordingly, the PC process and PS technology mutually improve the degradation performance of each other and therefore form synergistic effects in the PC-PS systems (Equations (1–6)):

$$\text{Photocatalysts} \xrightarrow{h\nu} h^+ + e^-, \quad (1)$$

$$e^- + O_2 \rightarrow \cdot O_2^-, \quad (2)$$

$$h^+ + H_2O \rightarrow \cdot OH, \quad (3)$$

$$S_2O_8^{2-} + e^- \rightarrow \cdot SO_4^- + SO_4^{2-}, \quad (4)$$

[1] Centre for Clean Environment and Energy and School of Environment and Science, Griffith University, Gold Coast, QLD 4222, Australia
[2] College of Materials and Energy, South China Agricultural University, Guangzhou 510643, China
[3] School of Biotechnology and Health Sciences, Wuyi University, Jiangmen 529020, China
[4] College of Materials and Chemical Engineering, Key Laboratory of Inorganic Nonmetallic Crystalline and Energy Conversion Materials, China Three Gorges University, Yichang 443002, China
[5] Key Laboratory of Materials Processing and Mold (Zhengzhou University), Ministry of Education, Zhengzhou 450002, China
* Corresponding authors (emails: zhangss@scau.edu.cn (Zhang SS); s.zhang@griffith.edu.au (Zhang SQ))

$$S_2O_8^{2-}+\cdot O_2^- \rightarrow \cdot SO_4^- + SO_4^{2-} + O_2, \quad (5)$$

$$h^+ / \cdot OH / \cdot SO_4^- + \text{dye} \rightarrow CO_2 + H_2O + \text{small molecule substance}. \quad (6)$$

To improve the performance of synergistic PC-PS degradation, designing and synthesizing highly efficient photocatalysts plays a critical role. In general, TiO_2 is the most commonly used photocatalyst material due to its appropriate band position, high chemical stability, low cost, and nontoxicity [7]. However, pristine TiO_2 photocatalysts can only be stimulated by UV irradiation because the bandgap of pristine TiO_2 is higher than 3.0 eV, which seriously impedes its utilization in low-cost and environmentally friendly solar energy applications [8]. According to previous studies, building heterojunctions between anatase and rutile TiO_2 effectively enhances solar energy utilization and PC efficiency [9–12]. Though the energy level position of the anatase/rutile heterophase junction is unclear, markedly improved separation rates of photogenerated electrons and holes have been experimentally verified [13–15]. Hydrogenation is another simple method for extending the absorption spectrum of TiO_2-based materials into the visible light region by bringing a disordered layer and oxygen vacancies into photocatalysts [16,17]. On one hand, the synergistic effect of the disordered layer and oxygen vacancies can narrow the bandgap of TiO_2 by introducing a new energy state below the bottom of the conduction band [18]; on the other hand, the electrochemical performance of the photocatalysts can be enhanced after a hydrogenation process, which promotes the separation of photogenerated electron-hole pairs [19,20].

Many studies have confirmed that device design also plays a crucial role in improving the efficiency and reducing the cost of PC reactors [21–23]. A thin-layer reactor, which minimizes the thickness of the aqueous solution and the distance between the irradiation source and photocatalysts, is a promising device design for effective utilization of irradiation [24]. According to Beer's Law, light loss in aqueous solution is inevitable (Equation (7)):

$$A = \varepsilon bc, \quad (7)$$

where A is the absorbance of light; ε is the molar absorptivity; b is the thickness of aqueous solution, and c is the electrolyte concentration. It can be directly inferred from Equation (7) that reducing the thickness of the aqueous solution can directly minimize the light loss in the electrolyte, which demonstrates that the thin-layer reactor will further improve the performance of PC dye degradation.

In this work, a highly efficient, scalable, portable, and low-cost wastewater treatment device was designed for small-scale textile plants at remote sites. Hydrogenated anatase branched-rutile TiO_2 nanorod (H-AB@RTNR) photocatalysts were fabricated and applied to improve the degradation efficiency of rhodamine B (RhB) under visible light irradiation. The effects of mixed-phase TiO_2 and oxygen vacancies generated by the hydrogenation process on the PC pathways were investigated. In addition, the introduction of PS into the PC system synergistically promoted the degradation efficiency of RhB. A thin-layer reactor was designed and built for the practical application of the PC-PS technology, which improved the efficiency, scalability, portability and cost-effectiveness of the reactor. The designed thin-layer reactor circulating flux of 5 L h^{-1} is capable of fully degrading 1 L RhB solution (20 mg L^{-1}) in 120 min with a high reaction rate constant of 0.0221 min^{-1}. Moreover, the thin-layer reactor showed excellent PC degradation capacity for real textile mill wastewater with good removal rates of total organic carbon (TOC, 62.3%) and chemical oxygen demand (COD, 74.8%) in 240 min operation with a circulating flux of 5 L h^{-1}.

EXPERIMENTAL SECTION

Materials and reagents

Fluorine-doped tin oxide (FTO) glass (with a resistance of 8 Ω per square and a thickness of 2.2 mm) was purchased from Delta Technologies Limited (USA) and used as a substrate for TiO_2 film growth. Tetrabutyl titanate (97%) was supplied by Sigma-Aldrich (USA) and employed as the precursors of TiO_2. RhB of commercial-grade was obtained from Sigma-Aldrich (USA). The characteristics of RhB are displayed in Table S1. Other chemical reagents, including hydrochloric acid (HCl, 36.5% by weight), boric acid (H_3BO_3), ammonium hexafluo-rotitanate ($[NH_4]_2TiF_6$), and sodium nitrate ($NaNO_3$) were of analytical grade and purchased from Sigma-Aldrich (USA). All reagents obtained from Sigma-Aldrich were used as received without further treatment unless otherwise stated. High-purity distilled water (Millipore Corp., 18 MΩ cm) was used in the preparation and dilution of solutions. The real water sample was taken from a textile mill in Queensland, Australia, and represents the original disposal from the textile furnishing process. The sample was stored in a refrigerator at 4°C according to standard method guidelines. The physiochemical properties of the real water sample are displayed in Table S2.

Synthesis of photocatalysts

Rutile TiO_2 nanorod arrays (RTNRs) were prepared according to a previously reported method [25]. Briefly, 20 mL distilled water was mixed with 20 mL HCl (11.9 mol L^{-1}) under vigorous stirring for 20 min. Then, 0.5 mL tetrabutyl titanate (2.94 mol L^{-1}) was added into the well-mixed solution. After stirring for another 20 min, the solution was transferred into a Teflon-lined stainless steel autoclave. Two pieces of well-cleaned FTO glass were half-immersed in the as-prepared solution and heated at 180°C for 12 h in an oven. To synthesize anatase RTNRs (AB@RTNRs), the RTNRs were put into a mixed solution consisting of 24.1 mol L^{-1} H_3BO_3 and 5.3 mol L^{-1} $[NH_4]_2TiF_6$ and subjected to hydrothermal treatment at 60°C for 24 h. The as-prepared samples were cooled to room temperature naturally, then washed several times with distilled water and dried in air. The hydrogenation process was conducted at 200°C in a tube furnace with a mixed gas flow consisting of 5% hydrogen and 95% argon for 1 h to obtain hydrogenated rutile nanorods (H-AB@RTNRs).

Characterizations

The nanostructured morphology was characterized by scanning electron microscopy (SEM, LEO 1530VP, Germany). The crystallographic phase and structure of photocatalysts were tested by X-ray diffraction (XRD) with an X-ray diffractometer (D/max-IIIA, Japan). The Raman spectra were obtained on a Renishaw in Via Raman microscope. X-ray photoelectron spectrophotometer (XPS) analysis was carried out with a Krato Axis Ultra DLD spectrometer with Al Kα X-ray ($h\nu$ = 1486.6 eV) at 15 kV and 150 W to characterize the chemical nature of the Ti and O states. Electron paramagnetic resonance (EPR) spectra were obtained with an E500 (Bruker, Germany) at 77 K and a radiofrequency of 9.442 GHz. UV-visible (UV-vis) spectra were obtained with a UV-vis spectrophotometer (Agilent Cary 300, USA) to characterize the bandgap energy of photocatalysts. The incident photo-to-current conversion efficiency (IPCE) spectra were obtained *via* an Oriel's QEPVSI-b monochromator system (Oriel Cornerstone™, USA). Fluorescence (FL) spectra were characterized *via* an F-4500 spectrophotometer (Hitachi, Japan) with an excitation wavelength of 260 nm. To evaluate the charge transportation situation, electrochemical impedance spectroscopy (EIS) testing was carried out under open-circuit voltage, with a 1.0 mol L^{-1} NaOH solution, with frequency ranging from 10 mHz to 1 MHz, and an amplitude of 5 mV on a CHI 660e electrochemical station (CH Instruments™, USA). Mott-Schottky (M-S) analysis was performed with a potential increment of 5×10^{-2} V, an amplitude of 5×10^{-3} V, and a frequency of 1 kHz.

Dye degradation performance measurement

The evaluation of liquid-phase PC oxidation of RhB was carried out in XPA-system Photochemical Reactors (Nanjing, China). The degraded RhB concentration was analyzed using a Cary 50 spectrophotometer (Varian Co., USA). The percentage of degradation was reported as C/C_0. C is the absorption of RhB at each irradiated time interval of the maximum peak of the absorption spectrum, and C_0 is the absorption of the initial concentration when adsorption/desorption equilibrium is achieved. The TOC and COD represent the amounts of organic compounds in the water sample. The TOC was tested with TOC-V_{CPN} Total Organic Carbon Analyzer (Shimadzu Corp., Japan), and the COD value was examined by an EPA-approved COD analyzer (Merck NOVA 30, USA). The PC dye degradation performance of H-AB@RTNRs was also tested with a homemade thin-layer cell system (Figs S1 and S2). The optical-electronic parameters and spectrum of the LED panel are displayed in Table S3. The details of the homemade thin-layer cell system are available in the Supplementary information.

RESULTS AND DISCUSSION

Materials characterization

Crystalline phase structure and morphology characterization

The crystalline nature and phase of the as-prepared nanocomposite photocatalysts were analyzed by XRD (Fig. 1a). After subtracting the diffraction peaks from FTO glass, the XRD peaks of the pure TiO_2 (RTNRs) were observed at 2θ = 25.6°, 36.1°, 41.2°, 54.3°, 62.8°, and 69.2°, which correspond to the characteristic peaks of tetragonal rutile crystalline phase (ICDD No. 88-1175). The results prove that pure rutile TiO_2 photocatalysts were synthesized on the surface of FTO glass. In the patterns of AB@RTNRs and H-AB@RTNR nanocomposites, new diffraction peaks in addition to the peaks of rutile TiO_2 were simultaneously observed at 2θ = 25.1°, 38.2°, and 47.7°, which are indexed to the characteristic peaks of anatase crystalline phase TiO_2 (ICDD No. 88-1175). The XRD patterns provide evidence that the anatase crystalline TiO_2 nanostructures exist in the branched-photocatalysts. Moreover, no additional peak was observed after the hydrogenation process, indicating that hydro-

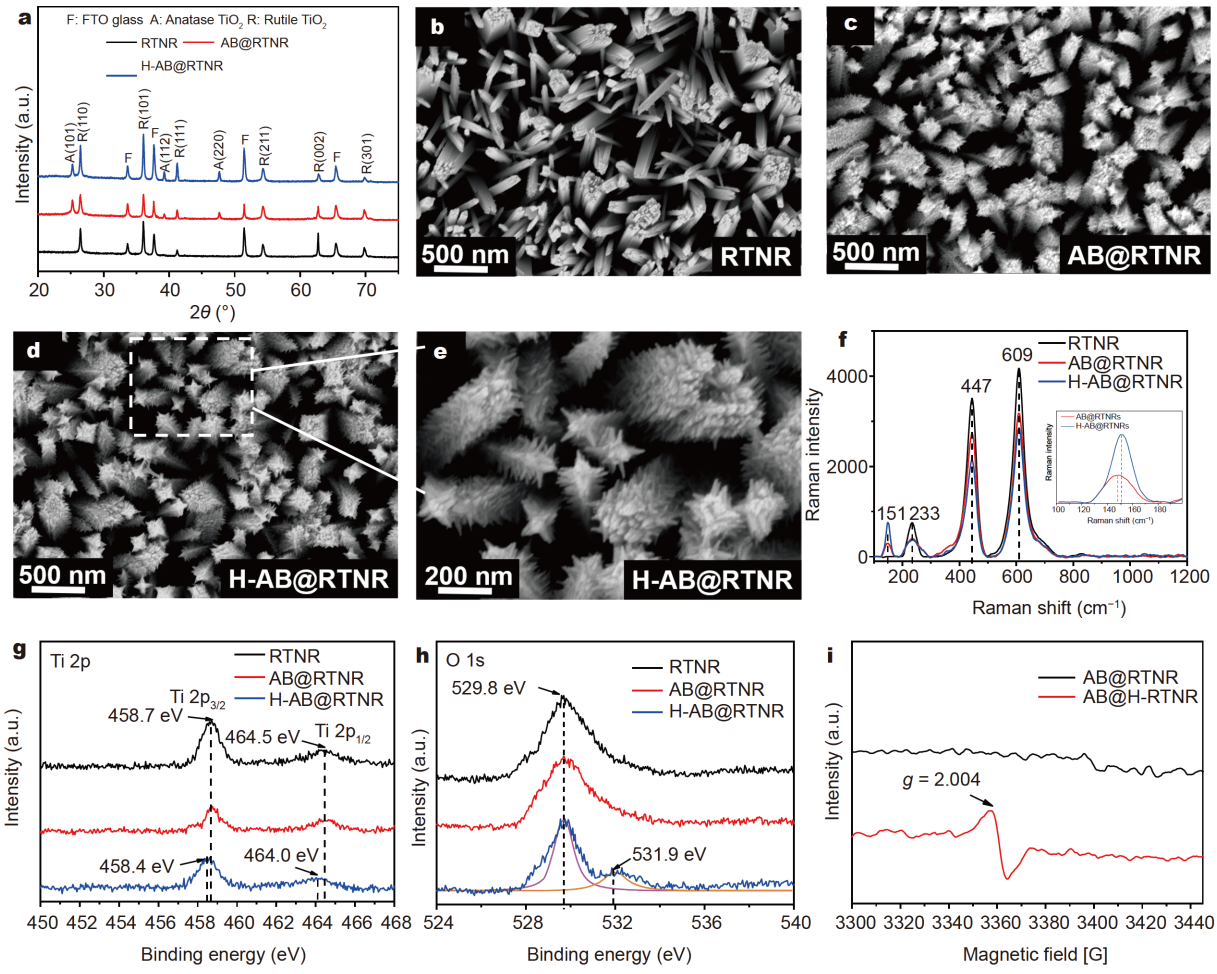

Figure 1 (a) XRD patterns; (b–e) FESEM surface morphologies; (f) Raman spectra (the inset exhibits the enlarged view of E_g peaks in the Raman spectra); XPS spectra for (g) Ti 2p and (h) O 1s; (i) EPR spectra of the as-prepared photocatalysts.

genation does not affect the crystal phase structure of the as-prepared materials. As a result, the diffraction peaks of the samples in Fig. 1a concur with the reports of rutile and anatase TiO_2 crystals in the literature [7,26].

The microstructure and surface morphology of the as-prepared nanocomposite were observed using field emission FEM (FESEM), with the results displayed in Fig. 1b–e. As revealed in Fig. 1b, smooth rutile TiO_2 nanorods with a length of 1.5 μm and a diameter of 200 nm were grown on FTO glass *via* a hydrothermal process. After the growth of anatase TiO_2 on the surface of the nanorods, branch-like TiO_2 were observed around the nanorods (Fig. 1c). The anatase branches were vertically grown and uniformly distributed on the surface of the nanorods, inferring that the surface area for absorbing light of branched nanorods was larger than that of RTNRs, which favours light absorption and extends the active reaction area. Fig. 1d and e display the morphology of the photocatalysts after the hydrogenation process, which is denoted as H-AB@RTNRs. It can be observed from the FESEM images that the hydrogenation process does not change the morphology of the photocatalysts.

Raman spectra were obtained to characterize the structural features and the vibrational modes of the as-prepared samples (Fig. 1f). Generally, in all photocatalyst patterns, three diffraction peaks centered at 233, 447, and 609 cm^{-1} were observed, which correspond to the Raman-active modes of rutile phase TiO_2 [27]. For the materials after the growth of anatase branches, a new peak appeared at 151 cm^{-1} which is indexed to the characteristic peaks of symmetric stretching vibrations of oxygen atoms in the O–Ti–O bond in anatase phase TiO_2. As shown in the inset in Fig. 1f, the E_g Raman peak at 151 cm^{-1} from the sample before hydrogenation shifted to a slightly

higher wavenumber after the hydrogenation process. The phenomenon can be attributed to the replacement of Ti ions which facilitates the formation of oxygen vacancies in hydrogenated materials because of the drop in O/Ti ratio [28,29].

Surface electron analysis

XPS analysis was conducted to confirm the detailed surface composition and elemental valence states of the as-prepared nanocomposite. As can be observed in Fig. 1g, the peaks located at 458.7 and 464.5 eV correspond to Ti $2p_{3/2}$ and Ti $2p_{1/2}$, respectively. The results imply the Ti exists as Ti^{4+} without the presence of Ti^{3+} in the surface layer of RTNRs and AB@RTNRs. After the hydrogenation process, the major peaks of XPS spectra shifted to 458.4 and 464.0 eV for Ti $2p_{3/2}$ and Ti $2p_{1/2}$, respectively, indicating the generation of Ti^{3+} on the surface layer of hydrogenated samples [25]. The O 1s spectra of the as-prepared photocatalysts are presented in Fig. 1h. The major peak at 529.8 eV in the O 1s spectrum provides evidence of the presence of Ti–O bonds in all the three as-prepared samples [30]. After the hydrogenation process, a new peak was obtained by deconvolution of the XPS spectrum of H-AB@RTNRs. The new peak appearing at 531.9 eV is attributed to Ti–OH bonds in H-AB@RTNRs, indicating that oxygen vacancies are formed during the hydrogenation process [31].

EPR analysis was applied to further illustrate the oxygen vacancies and Ti^{3+} on the surface layer of the photocatalysts (Fig. 1i). Before the hydrogenation, no significant major peaks were observed in the EPR spectrum of AB@RTNRs. Conversely, the hydrogenated samples exhibited a noticeable signal at the proportionality factor (g) value of 2.004, further proving the increase of oxygen vacancies and Ti^{3+} after the hydrogenation process. The results were compatible with the Raman and XPS patterns, which all provided evidence of the increased oxygen vacancies and Ti^{3+} on the surface layer of the photocatalysts. The detected oxygen vacancies and Ti^{3+} explain the superior PC performance of H-AB@RTNRs because those intrinsic defects significantly extend the light absorption range to the visible light region and facilitate the separation of photoinduced charge carriers, which therefore enhances the PC efficiency of the photocatalysts [32].

Optical features

The optical features of the materials were examined by UV-vis spectroscopy to investigate the light-harvesting ability of the as-prepared materials (Fig. 2a). As shown in the UV-vis spectra, the RTNRs only exhibit strong absorbance in the UV area, while the visible-light absorption was the lowest among all the three photocatalysts owing to its wide bandgap. The AB@RTNR sample displayed a noticeable increase in UV light absorption and a little enhancement in the visible light region. This phe-

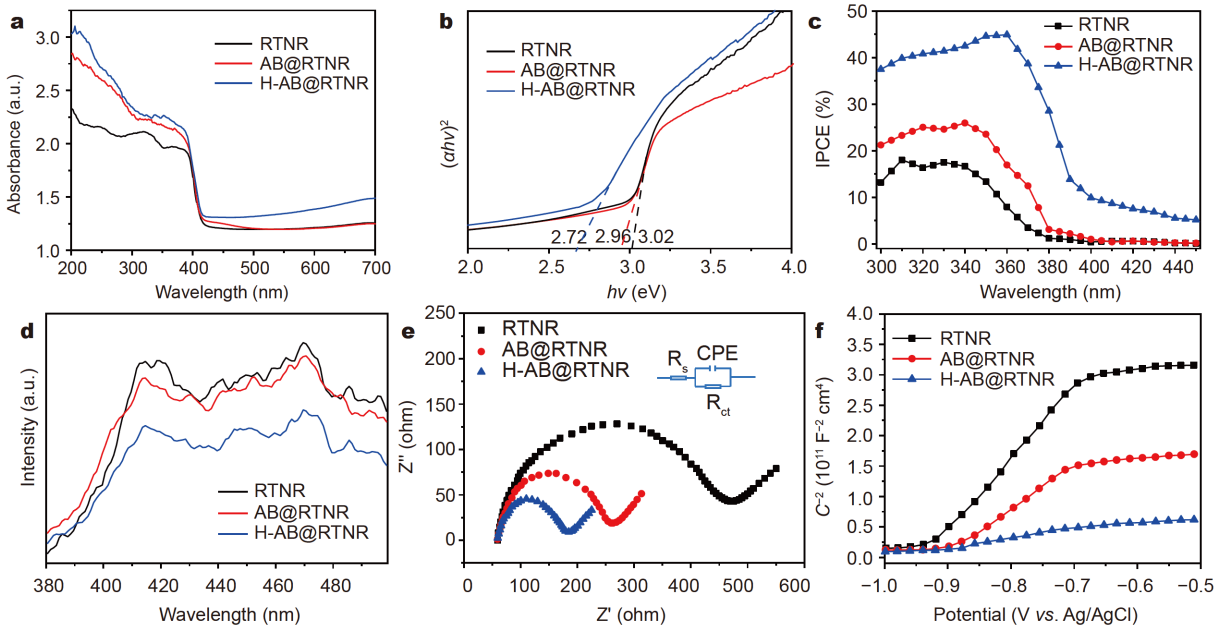

Figure 2 (a) UV-vis absorbance spectra; (b) Tauc plots derived from (a); (c) IPCE plots measured at 1.02 V *vs.* RHE applied bias; (d) FL, (e) EIS and (f) M-S spectra of RTNRs, AB@RTNRs, and H-AB@RTNRs.

nomenon could be attributed to the enlarged specific surface area from the branched structure and the alignment of different energy level positions of anatase and rutile, which slightly decrease the bandgap energy of the photocatalysts [15]. After the introduction of oxygen vacancies by the hydrogenation process, the H-AB@RTNR photocatalysts showed enhanced absorption in both UV light region and visible light region, which is consistent with the previous report [33]. The superior performance in light absorption of H-AB@RTNRs can be attributed to the narrowing of the bandgap by the introduction of oxygen vacancies and Ti^{3+} *via* the hydrogenation process as well as the enhanced light-harvesting capability of the branched structure. The results of H-AB@RTNR samples show impressive PC efficiency compared with the pristine RTNRs sample under visible-light irradiation due to the synergistic effects between the hydrogenation process and branched morphology.

To further investigate the bandgap energy of the as-prepared samples, the Tauc plots (Fig. 2b) were derived from the UV-vis spectra with the Tauc equation (Equation (8)) [34]:

$$(\lambda h\nu)^n = A(h\nu - E_g), \tag{8}$$

where A represents a constant, $h\nu$ represents the energy of irradiation, λ represents the measured absorption coefficient, and n equals 0.5 because the TiO_2 bandgap type is indirect [35]. The E_g of the as-prepared samples were obtained by extrapolation of the linear parts of the Tauc plots. As can be observed in Fig. 2b, the estimated E_g value for H-AB@RTNRs (E_g ~ 2.72 eV) is narrower than that of RTNRs (E_g ~ 3.02 eV) and AB@RTNRs (E_g ~ 2.96 eV). Therefore, the results further suggest that the bandgap of the as-prepared samples decrease with the introduction of oxygen vacancies and Ti^{3+} *via* the hydrogenation process, leading to enhanced light absorption in the region of visible light.

To investigate the quantum efficiency of the as-prepared photocatalysts, IPCE spectra were obtained and are exhibited in Fig. 2c. In the UV light region (before the wavelength of 380 nm), the H-AB@RTNRs exhibited the highest IPCE value among all the photocatalysts. Furthermore, the AB@RTNRs samples also showed an obvious light response within the visible light region (400–450 nm). This phenomenon could result from the synergistic effects between the well-aligned bandgap of mixed-phase TiO_2 and oxygen vacancies brought by the hydrogenation process.

The bandgap energy and recombination rate of charge carriers were investigated by FL spectra (Fig. 2d). Two major peaks were observed at the wavelength of 413 and 471 nm, which are equivalent to 3.00 and 2.63 eV, respectively. The first peak appearing at 413 nm is referred to as the bandgap energy of rutile TiO_2 (3.02 eV), which proves that the photocatalysts were basically composed of the rutile phase TiO_2. It could be observed that the intensity of the FL spectra of the branched structure (AB@RTNRs and H-AB@RTNRs) is more potent than that of the non-branched structure (RTNRs) in the range of 380–390 nm. The phenomenon could be explained by the introduction of anatase branches with higher bandgap energy (3.2 eV), which correspond to the wavelength of 387 nm. However, the proportion of the anatase branch was comparatively low compared with rutile nanorods, so no major characteristic peaks corresponding to anatase phase TiO_2 were observed at 387 nm. The FL spectra integral intensities of H-AB@RTNRs were lower than those of other as-prepared samples, implying that the recombination rate of photogenerated charge carriers for H-AB@RTNRs was the lowest among all the as-prepared photocatalysts.

Electrochemical properties

EIS was used to study the interfacial PEC properties, such as recombination and transmission of charge carriers, on the interface between photocatalysts and electrolyte (Fig. 2e). The Nyquist plots of the RTNRs, AB@RTNRs, and H-AB@RTNRs were fitted to the proposed equivalent circuit, the simplified Randles cell, which is displayed in the inset of Fig. 2e. In the simplified Randles cell, CPE represents the double layer capacitance, R_s represents the solution resistance, and R_{ct} represents the charge-transfer resistance, which corresponds to the radius of arcs in the Nyquist plots. It could be also observed from Fig. 2e that the order of the radius of arcs for different photocatalysts was RTNRs < AB@RTNRs < H-AB@RTNRs, indicating that the transmission resistance of charge carriers in the interface between TiO_2 and electrolyte decreased after the modification of morphology and bandgap structure.

M-S plots were applied to investigate the flat band potentials (E_{fb}) and types of semiconductors (Fig. 2f). The M-S plots clearly illustrates that all the as-prepared samples are typical n-type semiconductors because of the positive slopes of the M-S curves [36]. The donor density (N_d) of all samples was calculated *via* Equation (9):

$$N_d = \frac{2/\mathrm{e}_0\varepsilon\varepsilon_0}{\mathrm{d}(1/C^2)/\mathrm{d}V}, \tag{9}$$

where e_0 represents the charge of an electron (1.602×10^{-19} C), ε represents the dielectric constant of rutile

TiO_2, ε_0 represents the permittivity of free space in vacuum (8.854×10^{-12} F m^{-1}), and $d(1/C^2)/dV$ represents the slope by extrapolating the linear parts of M-S curves. Considering the values of e_0, ε and ε_0 are constants, it could be easily inferred that N_d was inversely proportional to $d(1/C^2)/dV$. Consequently, the smallest slope value of H-AB@RTNRs indicates that the donor density of H-AB@RTNRs was the highest among all the photocatalysts, which arises from the intrinsic defects brought about by the hydrogenation of the mixed-phase TiO_2. The results were also compatible with the smallest arc radius of H-AB@RNTRs from the Nyquist plots.

Performance of dye degradation by different processes

PC degradation

PC degradation of the as-prepared photocatalyst was investigated by degrading RhB under visible light. As illustrated in Fig. 3a, the removal efficiency of the photolysis process without adding any photocatalyst was negligible. After the introduction of RTNR photocatalysts, 2.2% of the RhB was eliminated after 240 min, which was similar to the removal rate of bare photolysis, indicating that the bare RTNRs hardly respond to visible light. Moreover, the degradation rate of RhB by the AB@RTNRs was 5.2% after 240 min, which is only a slight improvement compared with the bare RTNRs, showing that branched structure and mixed-phase strategy could slightly narrow the bandgap of the photocatalyst and moderately responds to visible light. However, the enhancement was not significant and further modification of the bandgap energy is needed. The visible light responses of RTNRs and AB@RTNRs were consistent with the IPCE results (Fig. 2c). After the hydrogenation process, the H-AB@RTNRs outperformed all the other as-prepared photocatalysts with an RhB removal rate of 95.2% in 240 min under visible light irradiation. To gain more insights into the procedure of PC degradation on H-AB@RTNRs, UV-vis spectra of the solutions collected at different time intervals are exhibited in Fig. 3b. Since the intensity of absorption spectra gradually decreased with irradiation time and the position of major peaks did not shift horizontally, it could be inferred that the PC degradation process of RhB followed the aromatic ring-opening mechanism [37].

PC-PS degradation kinetics

The synergistic effects between photocatalysts and PS anions were investigated by adding potassium persulphate ($K_2S_2O_8$) into the aqueous solution. As shown in Fig. 3c, the degradation rates of RhB on all as-prepared samples significantly increased after adding

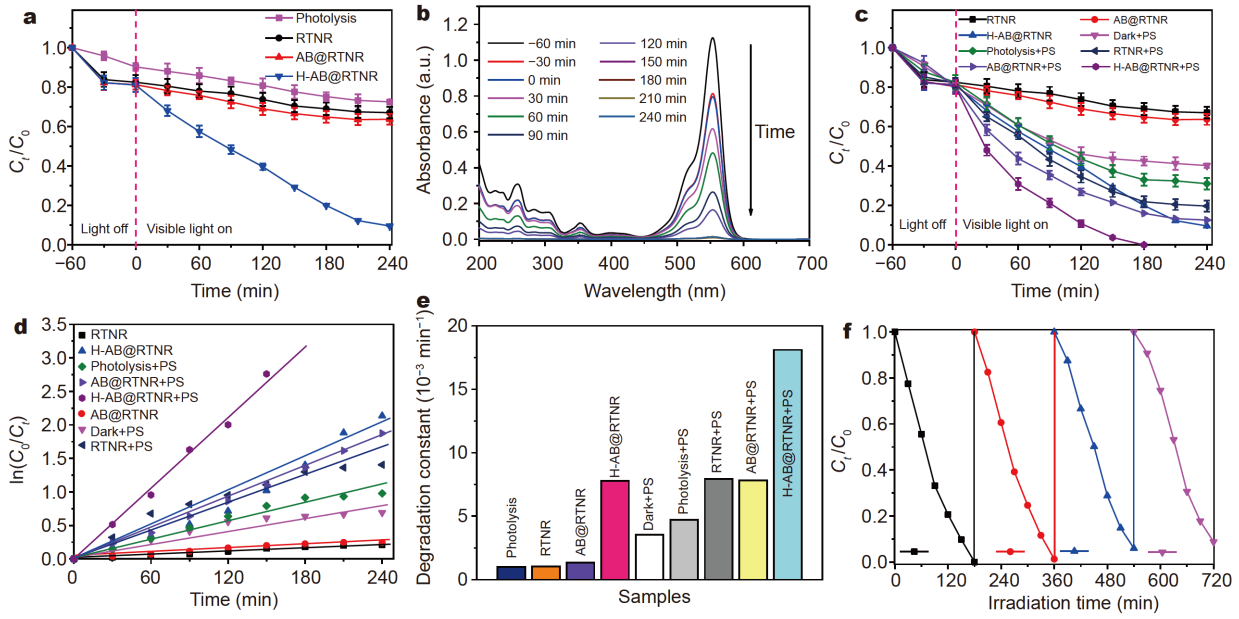

Figure 3 (a) PC degradation of RhB on the as-prepared photocatalysts; (b) UV-vis spectral changes for removal of RhB on the H-AB@RTNR; (c) PC degradation of RhB on the as-prepared photocatalysts in the presence and absence of PS; (d) Pseudo-first-order kinetics plots for the removal of RhB with the as-prepared samples; (e) the reaction rate constants of RhB for all the samples; (f) recycling runs for the H-AB@RTNRs photocatalyst on the PC-PS degradation of RhB.

1.48 mmol L^{-1} of $K_2S_2O_8$ solution, with the H-AB@RTNR photocatalysts achieving a degradation rate of 100% RhB after 180 min under visible light. The performance of dye degradation on different photocatalysts was explicitly investigated by using the pseudo-first-order kinetics model, as shown in Equation (10):

$$\ln(C_0/C) = kt, \quad (10)$$

where C_0 represents the initial concentration of dye solution, C represents the concentration of dye solution at time t, t represents the reaction time, and k represents the pseudo-first-order reaction rate constant. According to Equation (10), the kinetics plots for all the as-prepared photocatalysts, both in the presence and absence of PS anions, are exhibited in Fig. 3d. The linear relationship in kinetics plots provides evidence that the dye degradation process on the as-prepared samples obeyed the pseudo-first-order kinetics model. The degradation rates of all the samples were calculated from the kinetics plots and are displayed in Fig. 3e. It can be observed that the reaction rate constant of H-AB@RTNR photocatalyst with PS anions (18.2×10^{-3} min^{-1}) was much higher than that of RTNRs (7.4×10^{-3} min^{-1}) and AB@RTNRs (7.2×10^{-3} min^{-1}) as well as the samples without PS anions. The results prove that the synergistic effects between photocatalysts and PS anions could sharply increase the degradation rate of RhB on H-AB@RTNRs under visible light. The stability of photocatalysts during PC degradation is crucial for practical applications. Consequently, the recyclability of the H-AB@RTNRs for RhB degredation with PS anions was tested under identical conditions (Fig. 3f). The plots show no significant decrease in degradation performance of H-AB@RTNRs in the four recycled runs, exhibiting its superior stability in PC-PS degradation of RhB under visible light.

Design of PC-PS thin-layer reactor

The influential factors of the thin-layer cell system performance, such as the angle of the slanted bed and the thickness of aqueous solution, were investigated, and the results are displayed in Figs S3 and S4. The comparison of the performance of PC-PS degradation of RhB in a conventional bulk cell and the thin-layer cell was studied in the following experiments. RhB solutions with identical concentration (20 mg L^{-1}) were treated by these two processes, and the results are displayed in Fig. S5. As shown in Fig. S5a, the degradation rate of RhB in the thin-layer cell was higher than that of the conventional bulk cell. The result was attributed to the design of the thin-layer cell, which minimized the thickness of the water film layer and therefore reduced the light loss in aqueous solution. The pseudo-first-order kinetics plots are exhibited for intuitively illustrating the comparison of degradation performance between the two processes (Fig. S5b). The slope value of the pseudo-first-order kinetics plot for the thin-layer cell process was greater than that of the conventional bulk cell process, which proves that the thin-layer cell system could considerably improve the PC-PS degradation of RhB and achieved a degradation rate of 100% and a reaction rate constant of 0.0221 min^{-1} in 120 min under visible light.

PC-PS degradation mechanism

With the results presented above, a hypothetical explanation (Fig. 4) of the PC performance of H-AB@RTNRs in visible light region and the synergistic effects between H-AB@RTNRs and PS anions is proposed through two aspects. Firstly, from the perspective of photocatalysts, although the position of energy level alignment in mixed-phase anatase/rutile TiO_2 is controversial, it is widely accepted that the mixed-phase heterostructure could significantly improve the charge separation rate and slightly narrow the bandgap of photocatalysts, which favours the PC performance [13–15,38]. Furthermore, the hydrogenation process on the photocatalysts brought in abundant oxygen vacancies and Ti^{3+} in the surface layer of photocatalysts, which acted as a trapping site for capturing the photogenerated electrons and impeded the recombination of electron-hole pairs. The hydrogenation process also pronouncedly reduced the bandgap energy, which favoured its response to visible light. Secondly, from the perspective of synergistic effects in the PC-PS system, the reaction mechanism is displayed in Equations (1–6). Briefly, the photogenerated holes (h^+) reacted with H_2O to produce hydroxyl radicals (·OH), which possess high oxidation potential (E^0 = 2.80 V *vs.* NHE). The oxygen molecules (O_2) were reduced by photogenerated electrons (e^-) to produce superoxide anion radicals ($\cdot O_2^-$). Then e^- and $\cdot O_2^-$ further reacted with $S_2O_8^{2-}$ to produce $\cdot SO_4^-$, which possess a high oxidation potential (E^0 = 2.60 V *vs.* NHE). Therefore, the ·OH and $\cdot SO_4^-$ both played a principal role in the degradation process due to their superior oxidation potentials. The h^+ played a crucial role in generating ·OH by oxidizing water at the lower valence band of the photocatalysts. Moreover, $\cdot O_2^-$ was a major assistant in transforming the $S_2O_8^{2-}$ in solution into $\cdot SO_4^-$. In this way, the organic contaminant could be indiscriminately oxidized to the small-molecule substance. In turn, $S_2O_8^{2-}$ also acted as a trapping site for photogenerated electrons, which

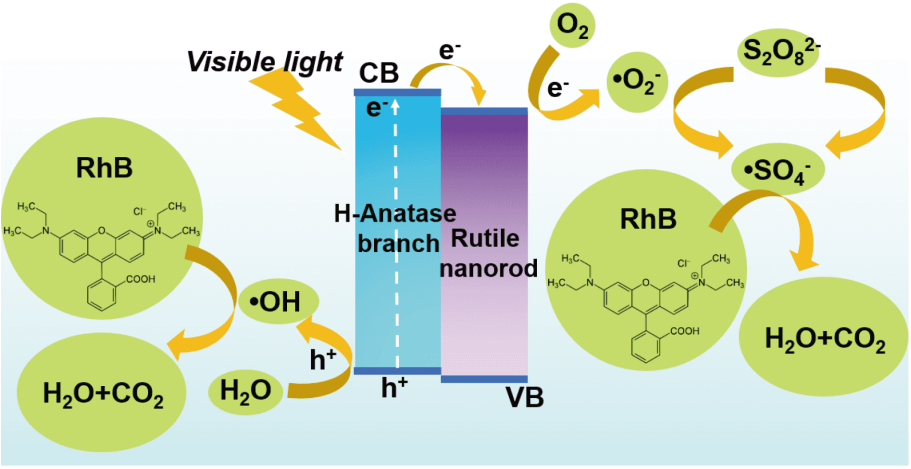

Figure 4 The mechanism of the synergistic PC-PS degradation of dye RhB.

improved the separation rate of photoinduced electron-hole pairs. In this way, the PS anions and H-AB@RTNR photocatalysts synergistically enhanced the degradation performance on RhB under visible light irradiation.

PC-PS degradation pathway of RhB

To investigate the degradation pathway of RhB under visible light irradiation, an LC/MS analysis was used to gain insights into the intermediate compounds generated during the PC-PS degradation process. Combining the results from the mass spectrograms of the intermediates during the degradation of RhB (Fig. S6) and the *m/z* values corresponding to the proposed intermediates' peaks (Table S4), a proposed degradation pathway can be acquired (Fig. 5), concurring with the results in previous studies [39]. There are four steps for RhB degradation. Firstly, the ethyl groups in RhB were attacked by radicals with high oxidation potential and experienced an *N*-de-ethylation process to generate phenyl oxonium intermediates (I–V). During the PC-PS process, five *N*-de-ethyl products were detected and their maximum peaks appeared in successive order, which demonstrated that the *N*-de-ethylation of RhB was a stepwise process. Secondly, in the chromophore cleavage process, the central carbon in the V was oxidized by active species, such as $\cdot SO_4^-$, $\cdot O_2^-$ and ·OH, generating major phenolic intermediates (VI–VIII). It can be also observed from Fig. S6 that during the whole degradation process, the chromophore cleavage of the RhB occurred simultaneously, reflecting the superior degradation ability of the PC-PS system. The photogenerated h^+, $\cdot O_2^-$, and ·OH as well as the PS-generated $\cdot SO_4^-$ directly attack the central carbon of the dye molecule. These active radicals could also react with the *N*-de-ethylation intermediates and generate the primary products, such as phthalic acid, benzoic acid, and 1,2-dimethylbenzene. The third process of RhB degradation was the ring opening process, where the low-molecular-weight intermediates generated in the previous process were further attacked by active radicals and formed the broken-ring intermediates (IX–XII). The last process was the mineralization of those broken-ring products to produce small molecule substances, such as CO_2 and H_2O.

PC-PS treatment of real wastewater sample

The practical applicability of the thin-layer cell system with the H-AB@RTNR photocatalysts was tested using a real wastewater sample discharged from a textile industry. As shown in Fig. S7, the COD and TOC removal of 74.8% and 62.3%, respectively, were achieved after 240 min degradation with H-AB@RTNRs in the thin-layer cell system under visible light irradiation. Moreover, the biodegradability variation of the wastewater sample was analyzed by calculating the average oxidation state (AOS) and carbon oxidation state (COS) by Equations (11) and (12):

$$\mathrm{AOS}=4-1.5\times \mathrm{COD/TOC}, \quad (11)$$

$$\mathrm{COS}=4-1.5\times \mathrm{COD/TOC}_0, \quad (12)$$

where COD and TOC represent the values recorded after 240 min degradation, TOC_0 represents the initial TOC value of the raw wastewater sample. The AOS and COS values varied within ± 4, which represent the most oxidized form (CO_2) and the most reduced form (CH_4) of

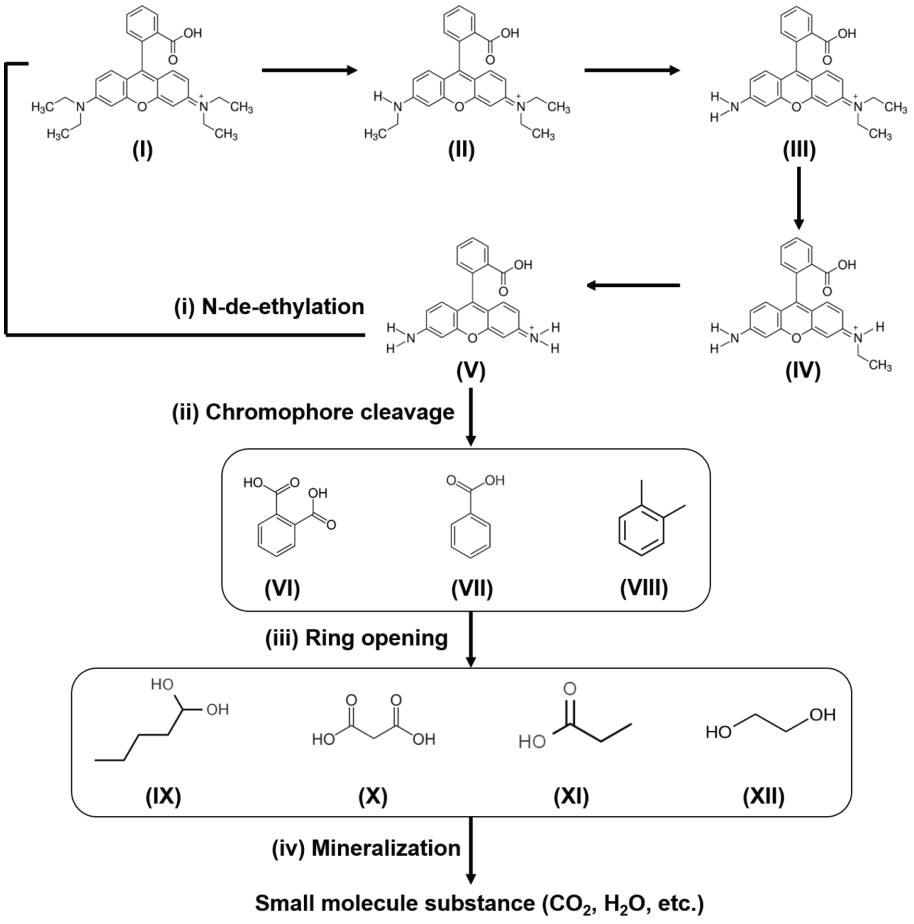

Figure 5 Proposed degradation pathway and intermediates during RhB degradation reaction with H-AB@RTNRs under visible light irradiation.

organic compounds. According to the experimental results, the AOS value was calculated to be 1.25 for raw wastewater samples. After a 240-min treatment process, the AOS and COS values of the solution were 2.16 and 3.31, respectively, which demonstrated that the biodegradability of raw wastewater was enhanced after PC-PS degradation in the thin-layer cell system.

CONCLUSION

A comprehensive study on designing a highly efficient, scalable, portable, and low-cost wastewater treatment and purification device for small-scale textile plants was carried out, and several conclusions are summarized as follows. Firstly, to improve the efficiency of contaminant degradation and reduce the cost of the operating device, the H-AB@RTNRs nanocomposites were successfully fabricated *via* a hydrothermal route. The H-AB@RTNRs were characterized by different methods to prove that the photocatalysts possessed abundant oxygen vacancies and Ti^{3+}, which facilitated the separation rate of electron-hole pairs and enhanced the light absorption in the visible region. In this way, clean and low-cost solar energy can be utilized for wastewater treatment with H-AB@RTNRs. Secondly, the introduction of PS anions into the PC degradation process enables the reactor to degrade refractory organic contaminants that could not be achieved by the PC process alone. The phenomenon can be attributed to the synergistic effects between H-AB@RTNRs and PS anions, where the photogenerated electrons act as the reactive sites for PS anions to generate active radicals ($\cdot SO_4^-$), which possess a high oxidation potential (E^0 = 2.60 V *vs.* NHE) and therefore exhibit superior degradation performance for persistent organic contaminants. Thirdly, the thin-layer cell design could reduce the light loss in the aqueous solution by minimizing the thickness of the water film between the irradiation source and photocatalysts, which maximizes light absorption by the photocatalysts and therefore achieves a better degradation

performance compared with the conventional bulk cell. The device design also improves the portability of the reactor and exhibits its potential for up-scaling. Finally, according to the results of the real wastewater treatment experiments, it can be shown that the H-AB@RTNRs photocatalysts and PC-PS degradation system in the thin-layer cell have significant potential for practical PC removal of organic dye contaminants in the environment.

Received 25 October 2020; accepted 30 December 2020; published online 12 March 2021

1 Sabri M, Habibi-Yangjeh A, Chand H, *et al.* Activation of persulfate by novel TiO_2/FeOCl photocatalyst under visible light: Facile synthesis and high photocatalytic performance. Separ Purif Tech, 2020, 250: 117268
2 Li Q, Hou X, Fang Z, *et al.* Construction of layered h-BN/TiO_2 hetero-structure and probing of the synergetic photocatalytic effect. Sci China Mater, 2020, 63: 276–287
3 Zhao Y, Kang S, Qin L, *et al.* Self-assembled gels of Fe-chitosan/montmorillonite nanosheets: Dye degradation by the synergistic effect of adsorption and photo-Fenton reaction. Chem Eng J, 2020, 379: 122322
4 Tang Q, An X, Lan H, *et al.* Polyoxometalates/TiO_2 photocatalysts with engineered facets for enhanced degradation of bisphenol A through persulfate activation. Appl Catal B-Environ, 2020, 268: 118394
5 Anipsitakis GP, Dionysiou DD. Radical generation by the interaction of transition metals with common oxidants. Environ Sci Technol, 2004, 38: 3705–3712
6 Li X, Huang X, Xi S, *et al.* Single cobalt atoms anchored on porous N-doped graphene with dual reaction sites for efficient Fenton-like catalysis. J Am Chem Soc, 2018, 140: 12469–12475
7 Zu M, Zheng M, Zhang S, *et al.* Designing robust anatase-branch@hydrogenated-rutile-nanorod TiO_2 as accurate and sensitive photoelectrochemical sensors. Sens Actuat B-Chem, 2020, 321: 128504
8 Liu L, Liu X, Chai Y, *et al.* Surface modification of TiO_2 nanosheets with fullerene and zinc-phthalocyanine for enhanced photocatalytic reduction under solar-light irradiation. Sci China Mater, 2020, 63: 2251–2260
9 He J, Du YE, Bai Y, *et al.* Facile formation of anatase/rutile TiO_2 nanocomposites with enhanced photocatalytic activity. Molecules, 2019, 24: 2996
10 Zhou T, Chen S, Li L, *et al.* Carbon quantum dots modified anatase/rutile TiO_2 photoanode with dramatically enhanced photoelectrochemical performance. Appl Catal B-Environ, 2020, 269: 118776
11 Ai C, Xie P, Zhang X, *et al.* Explaining the enhanced photoelectrochemical behavior of highly ordered TiO_2 nanotube arrays: Anatase/rutile phase junction. ACS Sustain Chem Eng, 2019, 7: 5274–5282
12 Zhong Y, Ma S, Chen K, *et al.* Controlled growth of plasmonic heterostructures and their applications. Sci China Mater, 2020, 63: 1398–1417
13 Miyagi T, Kamei M, Mitsuhashi T, *et al.* Charge separation at the rutile/anatase interface: a dominant factor of photocatalytic activity. Chem Phys Lett, 2004, 390: 399–402
14 Kawahara T, Konishi Y, Tada H, *et al.* A patterned TiO_2(anatase)/TiO_2(rutile) bilayer-type photocatalyst: Effect of the anatase/rutile junction on the photocatalytic activity. Angew Chem, 2002, 114: 2935–2937
15 Scanlon DO, Dunnill CW, Buckeridge J, *et al.* Band alignment of rutile and anatase TiO_2. Nat Mater, 2013, 12: 798–801
16 Wang X, Mayrhofer L, Hoefer M, *et al.* Facile and efficient atomic hydrogenation enabled black TiO_2 with enhanced photo-electrochemical activity *via* a favorably low-energy-barrier pathway. Adv Energy Mater, 2019, 9: 1900725
17 Xiao F, Zhou W, Sun B, *et al.* Engineering oxygen vacancy on rutile TiO_2 for efficient electron-hole separation and high solar-driven photocatalytic hydrogen evolution. Sci China Mater, 2018, 61: 822–830
18 Pan J, Dong Z, Wang B, *et al.* The enhancement of photocatalytic hydrogen production *via* Ti^{3+} self-doping black TiO_2/g-C_3N_4 hollow core-shell nano-heterojunction. Appl Catal B-Environ, 2019, 242: 92–99
19 Lu Y, Yin WJ, Peng KL, *et al.* Self-hydrogenated shell promoting photocatalytic H_2 evolution on anatase TiO_2. Nat Commun, 2018, 9: 2752
20 Zhuang G, Chen Y, Zhuang Z, *et al.* Oxygen vacancies in metal oxides: Recent progress towards advanced catalyst design. Sci China Mater, 2020, 63: 2089–2118
21 Bhatkhande DS, Pangarkar VG, Beenackers AACM. Photocatalytic degradation for environmental applications—A review. J Chem Technol Biotechnol, 2002, 77: 102–116
22 Zhao W, Wang X, Ma L, *et al.* WO_3/p-type-GR layered materials for promoted photocatalytic antibiotic degradation and device for mechanism insight. Nanoscale Res Lett, 2019, 14: 146
23 Li H, Long B, Ye KH, *et al.* A recyclable photocatalytic tea-bag-like device model based on ultrathin Bi/C/BiOX (X = Cl, Br) nanosheets. Appl Surf Sci, 2020, 515: 145967
24 Wang Y, Zu M, Zhou X, *et al.* Designing efficient TiO_2-based photoelectrocatalysis systems for chemical engineering and sensing. Chem Eng J, 2020, 381: 122605
25 Zhang S, Zhang S, Peng B, *et al.* High performance hydrogenated TiO_2 nanorod arrays as a photoelectrochemical sensor for organic compounds under visible light. Electrochem Commun, 2014, 40: 24–27
26 Lin J, Sun T, Li M, *et al.* More efficiently enhancing photocatalytic activity by embedding Pt within anatase–rutile TiO_2 heterophase junction than exposing Pt on the outside surface. J Catal, 2019, 372: 8–18
27 Wang CC, Chou PH. Effects of various hydrogenated treatments on formation and photocatalytic activity of black TiO_2 nanowire arrays. Nanotechnology, 2016, 27: 325401
28 Chen S, Li D, Liu Y, *et al.* Morphology-dependent defect structures and photocatalytic performance of hydrogenated anatase TiO_2 nanocrystals. J Catal, 2016, 341: 126–135
29 Ye K, Li K, Lu Y, *et al.* An overview of advanced methods for the characterization of oxygen vacancies in materials. TrAC Trends Anal Chem, 2019, 116: 102–108
30 Zhang X, Hu W, Zhang K, *et al.* Ti^{3+} self-doped black TiO_2 nanotubes with mesoporous nanosheet architecture as efficient solar-driven hydrogen evolution photocatalysts. ACS Sustain Chem Eng, 2017, 5: 6894–6901
31 Chen X, Liu L, Huang F. Black titanium dioxide (TiO_2) nanomaterials. Chem Soc Rev, 2015, 44: 1861–1885
32 Chen X, Liu L, Yu PY, *et al.* Increasing solar absorption for photo-

catalysis with black hydrogenated titanium dioxide nanocrystals. Science, 2011, 331: 746–750
33 Hu J, Zhang S, Cao Y, *et al.* Novel highly active anatase/rutile TiO_2 photocatalyst with hydrogenated heterophase interface structures for photoelectrochemical water splitting into hydrogen. ACS Sustain Chem Eng, 2018, 6: 10823–10832
34 Tauc J. Optical properties and electronic structure of amorphous Ge and Si. Mater Res Bull, 1968, 3: 37–46
35 Reyes-Coronado D, Rodríguez-Gattorno G, Espinosa-Pesqueira ME, *et al.* Phase-pure TiO_2 nanoparticles: anatase, brookite and rutile. Nanotechnology, 2008, 19: 145605
36 Yan J, Han X, Qian J, *et al.* Preparation of 2D graphitic carbon nitride nanosheets by a green exfoliation approach and the enhanced photocatalytic performance. J Mater Sci, 2017, 52: 13091–13102
37 Asadzadeh-Khaneghah S, Habibi-Yangjeh A, Seifzadeh D. Graphitic carbon nitride nanosheets coupled with carbon dots and BiOI nanoparticles: Boosting visible-light-driven photocatalytic activity. J Taiwan Institute Chem Engineers, 2018, 87: 98–111
38 Li K, Lu X, Zhang Y, *et al.* Bi_3TaO_7/Ti_3C_2 heterojunctions for enhanced photocatalytic removal of water-borne contaminants. Environ Res, 2020, 185: 109409
39 Isari AA, Payan A, Fattahi M, *et al.* Photocatalytic degradation of rhodamine B and real textile wastewater using Fe-doped TiO_2 anchored on reduced graphene oxide (Fe-TiO_2/rGO): characterization and feasibility, mechanism and pathway studies. Appl Surf Sci, 2018, 462: 549–564

Acknowledgements This research was supported by Griffith University PhD scholarships, the National Natural Science Foundation of China (22078118), and the Natural Science Foundation of Guangdong Province (2019A1515011138).

Author contributions Zu M, Zhang SS and Zhang SQ conceived the idea, designed and developed the experimental plan. Zu M performed the experiments, collected and processed the data, and wrote the manuscript. All the authors discussed the results, analyzed and interpreted the data, and participated in the preparation of the manuscript.

Conflict of interest The authors declare that they have no conflict of interest.

Supplementary information Experimental details and supporting data are available in the online version of the paper.

Meng Zu is currently a PhD student at the Centre for Clean Environment and Energy, School of Environment and Science, Griffith University, Australia. He received his Master degree from the Department of Civil and Environmental Engineering, Cornell University in 2016. His research interests include the design and development of functional nanomaterials for photoelectrocatalytic sensing and treatment of aquatic pollutants.

Shengsen Zhang obtained his PhD degree from South China University of Technology, China in 2012. He is now an associate professor at the College of Materials and Energy, South China Agricultural University, China. His research interests include the synthesis, modification, and characterization of nanostructured materials for wastewater purification, sensing, and energy conversion.

Shanqing Zhang obtained his PhD degree in electrochemistry in 2001 at Griffith University, Australia. He is now a professor at Griffith University. His research interests include energy conversion, energy storage, and environmental monitoring.

可见光光催化剂-过硫酸盐协同净化污水系统

祖萌[1], 张声森[2*], 刘长宇[3], 刘珀润[1], 李东升[4], 邢超[1,5], 张山青[1*]

摘要 本文报道了一种氢化金红石/锐钛矿混晶结构的TiO_2薄膜光催化材料(H-AB@RTNR)与过硫酸盐协同降解有机污染物的新方法，设计了一套薄层式反应器以提高该方法对污染物的降解效率，建立了可见光光催化剂-过硫酸盐协同净化污水系统. 实验结果表明，在可见光(λ>420 nm)的照射下，120分钟内可完全净化1 L浓度为20 mg L^{-1}的罗丹明B溶液，反应速率常数达到0.0221 min^{-1}. 在对实际工业废水的处理实验中，此系统也表现出优异的净化效果. 机理分析表明此系统优异的净化污水性能主要归功于反应中生成的大量硫酸根自由基 ($\cdot SO_4^-$)和羟基自由基 ($\cdot OH$). 最后本文对降解过程中的中间产物进行了分析，明确了降解有机物的反应路径.

